Harnefors, Lennart; Wang, Xiongfei; Chou, Shih-Feng; Bongiorno, Massimo; Hinkkanen, Marko; Routimo, Mikko

Asymmetric complex-vector models with application to VSC–grid interaction

Published in:
IEEE JOURNAL OF EMERGING AND SELECTED TOPICS IN POWER ELECTRONICS

DOI:
10.1109/JESTPE.2020.2972070

Published: 06/02/2020

Document Version
Peer-reviewed accepted author manuscript, also known as Final accepted manuscript or Post-print

Please cite the original version:
Harnefors, L., Wang, X., Chou, S.-F., Bongiorno, M., Hinkkanen, M., & Routimo, M. (2020). Asymmetric complex-vector models with application to VSC–grid interaction. *IEEE JOURNAL OF EMERGING AND SELECTED TOPICS IN POWER ELECTRONICS*, *8*(2), 1911-1921. Article 8985279. https://doi.org/10.1109/JESTPE.2020.2972070

Asymmetric Complex-Vector Models With Application to VSC–Grid Interaction

Lennart Harnefors, *Fellow, IEEE*, Xiongfei Wang, *Senior Member, IEEE*, Shih-Feng Chou, *Member, IEEE*, Massimo Bongiorno, *Senior Member, IEEE*, Marko Hinkkanen, *Senior Member, IEEE*, and Mikko Routimo, *Member, IEEE*

***Abstract*—The properties of complex space-vector models for asymmetric three-phase systems are investigated in this paper. Most importantly, three alternative methods for stability analysis of asymmetric closed-loop systems are presented. The end results avoid the usage of matrix manipulations. It is shown how the theory can be applied to modeling and stability analysis of a grid-connected voltage-source converter (VSC). The methods are compared using numerical examples.**

***Index Terms*—Complex space vectors, complex transfer functions, converter control, passivity, stability.**

I. Introduction

SYMMETRIC (balanced) three-phase dynamic systems can be modeled using complex space vectors together with complex transfer functions [1]. This allows a single-input single-output (SISO) notation, even though the system in reality is multi-input multi-output (MIMO), since each space vector has two components.

Conversely, the input admittance of a grid-connected voltage-source converter (VSC), as seen from the point of common coupling (PCC), has in general asymmetric (also called unsymmetric or imbalanced) properties [2]. This traditionally necessitates MIMO models using real space vectors and 2×2 transfer function matrices [3]–[5]. Such modeling methods are well established [6]–[9]; yet, they add complexity relative SISO models. For stability analysis, the conventional Nyquist criterion (NC) is replaced by the generalized Nyquist criterion (GNC) [10], [11]. Matrix modeling of the grid impedance is needed, which is inconvenient particularly for a symmetric grid, where a SISO model suffices.

Steps toward generalizing complex-vector theory to asymmetric models, including VSC modeling and analysis, have been taken. In [1], it is shown how a 2×2 transfer function matrix can be decomposed into two complex transfer functions, respectively for the (here called) symmetric and antisymmetric parts. An *asymmetric complex-vector SISO model* is obtained. In [12], it is suggested to neglect the antisymmetric part. Avoiding this simplification, a MIMO scheme is considered in a series of papers by Rygg et al., [13]–[16]. The scheme is in [13] called modified sequence domain, but is here, for consistency with the aforementioned SISO model, called an *asymmetric complex-vector MIMO model*. Compared to the real-vector MIMO model, certain benefits are gained, including the usage of SISO techniques for stability analysis and grid-impedance modeling. A similar model, but in the stationary $\alpha\beta$ frame rather than in the synchronous dq frame, is proposed in [17].

In this paper, further results for the asymmetric complex-vector SISO and MIMO models are presented in Section II. They include expressions for cascading two SISO models and certain properties of the generic transfer function matrix of the MIMO model. The method for modeling of grid-connected VSCs of [12] is revisited and clarified concerning the antisymmetric part. In addition, the principles of [2] for dissipation and passivity of a MIMO model are briefly reprised. It is shown that the measure of passivity, here called the *passivity index*, can be conveniently expressed in the transfer functions of the asymmetric complex-vector SISO model.

The most important contribution is the consideration in Section III of three alternative methods for closed-loop stability analysis using the asymmetric complex-vector models. Method 1 extends the approach of [12] by taking also the antisymmetric part into account. The closed-loop system is separated into a symmetric inner loop and an antisymmetric outer loop. Stability is analyzed by applying the NC to both loops. (Another method using cascaded loops for stability analysis of grid-connected VSCs—but not relying on complex vectors—is proposed in [18], [19].) Methods 2 and 3 respectively utilize the eigenvalue and determinant GNC variants applied to the asymmetric complex-vector MIMO model. Expressions which solely use the transfer functions of the corresponding SISO model are derived, thereby obviating matrix manipulations. Methods 2 and 3 are close in spirit to the SISO approach for stability analysis in [15], but they are generic for any asymmetric system, whereas in [15] the interconnection of two impedances is considered. Although grid-connected VSCs are the foremost application, there are potentially many other, such as subsynchronous-oscillation studies [20].

In Section IV, finally, the three methods for stability analysis of Section III are compared using illustrative numerical examples (one of them verified experimentally), as applied to

This work was supported in part by ABB.

L. Harnefors is with ABB AB, Corporate Research, Västerås, Sweden (e-mail: lennart.harnefors@se.abb.com).

X. Wang and S.-F. Chou are with the Department of Energy Technology, Aalborg University, Aalborg, Denmark (e-mail: xwa@et.aau.dk, shc@et.aau.dk).

M. Bongiorno is with the Department of Electrical Engineering, Chalmers University of Technology, Göteborg, Sweden (e-mail: massimo.bongiorno@chalmers.se).

M. Hinkkanen is with the Department of Electrical Engineering and Automation, Aalto University, Espoo, Finland (e-mail: marko.hinkkanen@aalto.fi).

M. Routimo is with ABB Oy Drives, Helsinki, Finland (e-mail: mikko.routimo@fi.abb.com).

the VSC model of Section II. It is verified that all methods give identical results concerning stability vs. instability, while they have different properties regarding how the information is presented. Whereas Method 2 may be the most straightforward to use, Method 1 provides valuable insight into the mechanisms causing instability and the risk thereof. Method 3 is found to be less desirable, since the resulting Nyquist curve often is difficult to interpret, and can tentatively be dismissed from further studies.

II. Complex-Vector Modeling of Asymmetric Systems

Complex space vectors and their associated complex transfer functions (denoted by bold letters) facilitate modeling of symmetric systems. Assuming modeling in the dq frame, with the generic input and output vectors $\mathbf{u} = u_d + ju_q$ and $\mathbf{y} = y_d + jy_q$ and the generic transfer function $\mathbf{G}(s) = G_d(s) + jG_q(s)$, we have[1]

$$\mathbf{y} = \mathbf{G}(s)\mathbf{u}. \tag{1}$$

Despite that each vector accounts for two signals, the d and q components, a SISO notation is facilitated. By resolving the d and q components, the MIMO correspondence to (1) is obtained, using two-row real space vectors and a 2×2 transfer function matrix (denoted by italic letters) as

$$\underbrace{\begin{bmatrix} y_d \\ y_q \end{bmatrix}}_{y} = \underbrace{\begin{bmatrix} G_{dd}(s) & G_{dq}(s) \\ G_{qd}(s) & G_{qq}(s) \end{bmatrix}}_{G(s)} \underbrace{\begin{bmatrix} u_d \\ u_q \end{bmatrix}}_{u} \tag{2}$$

with

$$G_{dd}(s) = G_{qq}(s) = G_d(s) \qquad G_{qd}(s) = -G_{dq}(s) = G_q(s). \tag{3}$$

By lifting the restriction (3), allowing four unique matrix elements, asymmetric systems—such as VSCs and salient-pole synchronous machines—can be modeled as well. However, then (1) no longer suffices, which precludes modeling using complex vectors and a SISO notation.

A. Asymmetric Complex-Vector SISO Model

In [1] it is proposed to extend the SISO model (1) to asymmetric systems by using two parts, here called symmetric and antisymmetric, each having its own transfer function. The antisymmetric part takes the conjugated input signal, denoted by $(\cdot)^*$. With a cleaner notation than in [1], in the sense that subscripts are avoided, the model is expressed as

$$\mathbf{y} = \mathbf{G}(s)\mathbf{u} + \tilde{\mathbf{G}}(s)\mathbf{u}^*. \tag{4}$$

The block diagram in Fig. 1(a) illustrates (4) graphically (the dashed feedback loop is, at this stage, disregarded). With $\tilde{\mathbf{G}}(s) = \tilde{G}_d(s) + j\tilde{G}_q(s)$ in addition to $\mathbf{G}(s)$, (4) has four degrees of freedom. In [21], it is demonstrated how this model can be applied to various asymmetric systems.

The effect of the conjugation made in the antisymmetric part is illustrated particularly well for a steady-state frequency component in $\mathbf{u}$ which rotates counterclockwise, say $\mathbf{U}e^{j\omega t}$. The conjugation gives rise to a mirror component $\mathbf{U}^*e^{-j\omega t}$, rotating clockwise. Filtered through $\tilde{\mathbf{G}}(s)$, the mirror component adds to the output signal.

[1]The Laplace variable s shall be considered as the operator $s = d/dt$, where appropriate.

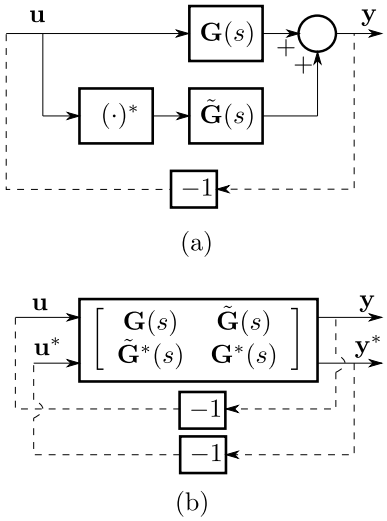

Fig. 1. (a) Asymmetric complex space-vector SISO model. (b) Corresponding MIMO model. The dashed lines show optional feedback loops which are considered in Section III.

The model (4) can be extended in various ways. Of particular importance is the cascade connection of two asymmetric systems, e.g., asymmetric admittance and impedance

$$\mathbf{i} = \mathbf{Y}(s)\mathbf{u} + \tilde{\mathbf{Y}}(s)\mathbf{u}^* \tag{5}$$

$$\mathbf{Y} = \mathbf{Z}(s)\mathbf{i} + \tilde{\mathbf{Z}}(s)\mathbf{i}^*. \tag{6}$$

Substituting (5) in (6) yields

$$\mathbf{Y} = \mathbf{Z}(s)[\mathbf{Y}(s)\mathbf{u} + \tilde{\mathbf{Y}}(s)\mathbf{u}^*] + \tilde{\mathbf{Z}}(s)[\mathbf{Y}(s)\mathbf{u} + \tilde{\mathbf{Y}}(s)\mathbf{u}^*]^* \tag{7}$$

which simplifies to (4) with

$$\mathbf{G}(s) = \mathbf{Z}(s)\mathbf{Y}(s) + \tilde{\mathbf{Z}}(s)\tilde{\mathbf{Y}}^*(s) \tag{8}$$

$$\tilde{\mathbf{G}}(s) = \mathbf{Z}(s)\tilde{\mathbf{Y}}(s) + \tilde{\mathbf{Z}}(s)\mathbf{Y}^*(s). \tag{9}$$

In a similar fashion, the input–output description of any asymmetric system or circuit, no matter how complex, can be reduced to the SISO model (4).

Remark 1: In the sequel, some equations explicitly involve the d and q components of a complex transfer function. They can be extracted according to [1]

$$G_d(s) = \frac{\mathbf{G}(s) + \mathbf{G}^*(s)}{2} \qquad G_q(s) = \frac{\mathbf{G}(s) - \mathbf{G}^*(s)}{2j}. \tag{10}$$

Remark 2: Observe that, when conjugating a complex transfer function as in (10), s is to be considered real. This means that care must be exercised when computing the frequency response of a conjugated transfer function, e.g., $\mathbf{G}^*(j\omega)$. Numerically, conjugation is more conveniently applied to the full frequency response, denoted as $[\mathbf{G}(j\omega)]^*$. From the rules of conjugation we have that $\mathbf{G}^*(s) = [\mathbf{G}(s^*)]^*$, and specifically for $s = j\omega$

$$\mathbf{G}^*(j\omega) = [\mathbf{G}(-j\omega)]^*. \tag{11}$$

This is straightforward to implement, e.g., in MATLAB. A vector representing $\mathbf{G}(j\omega)$ is first computed, with points symmetrically distributed for positive and negative ω. The vector representing $[\mathbf{G}(-j\omega)]^*$ is then obtained by applying the commands `fliplr` and `conj`.

B. Asymmetric Complex-Vector MIMO Model

Suppose that there is a mirror component already in the input signal. This is the case particularly when closing the feedback loop in Fig. 1(a), see Section III. The SISO model (4) then does not immediately reveal the couplings between the two components. To facilitate this, an extension to a corresponding MIMO model can be made by first conjugating (4) as $\mathbf{Y}^* = \mathbf{G}^*(s)\mathbf{u}^* + \tilde{\mathbf{G}}^*(s)\mathbf{u}$. The asymmetric complex-vector MIMO model (denoted by bold–italic letters) is then formed by combining (4) and its conjugate, collecting the original and conjugated (mirror) components in two-row vectors as [see Fig. 1(b)]

$$\underbrace{\begin{bmatrix} \mathbf{y} \\ \mathbf{y}^* \end{bmatrix}}_{\boldsymbol{y}} = \underbrace{\begin{bmatrix} \mathbf{G}(s) & \tilde{\mathbf{G}}(s) \\ \tilde{\mathbf{G}}^*(s) & \mathbf{G}^*(s) \end{bmatrix}}_{\boldsymbol{G}(s)} \underbrace{\begin{bmatrix} \mathbf{u} \\ \mathbf{u}^* \end{bmatrix}}_{\boldsymbol{u}}. \tag{12}$$

Models in the form (12) are extensively studied in [13]–[16]. Among other things, it is shown in [13] that $\boldsymbol{G}(s)$ can be obtained from $G(s)$ of the original real-vector MIMO model (2) via the linear transformation

$$\boldsymbol{G}(s) = \boldsymbol{T}G(s)\boldsymbol{T}^{-1}, \qquad \boldsymbol{T} = \frac{1}{\sqrt{2}}\begin{bmatrix} 1 & j \\ 1 & -j \end{bmatrix}. \tag{13}$$

$\boldsymbol{T}$ is unitary, i.e., $\boldsymbol{T}^{-1} = \boldsymbol{T}^H$, where the superscript H indicates transpose–conjugate (Hermitian conjugate). Transformation (13), although with the matrix $\boldsymbol{T} \to \boldsymbol{T}/\sqrt{2}$, was introduced already in the mid-1970s [20].

Some benefits of (12) relative (2) are stated in [13]–[16], among them that the off-diagonal elements of $\boldsymbol{G}(s)$ quantify the level of asymmetry. For the special case of a symmetric system they vanish, reducing (12) to (1) and its conjugate.

Another benefit of (12) is that $\boldsymbol{G}(s)$ has a restricted structure. Whereas the elements of $G(s)$ in (2) can be arbitrary, the diagonal and the off-diagonal elements of $\boldsymbol{G}(s)$ are identical, but conjugated. This fact is pointed out in [22], but yet it does not seem to be fully embraced in the literature. The reason for the restriction is that the information of the SISO model is duplicated in the MIMO model; the second row of (12) is the conjugate of the first row. The asymmetric complex-vector SISO and MIMO models are therefore complementary and carry exactly the same information. The main purpose of the MIMO model is as a tool for calculating results that cannot be obtained using the SISO model, as exemplified in the sequel.

As (12) is generic for any asymmetric system, it is not surprising that the restricted structure of $\boldsymbol{G}(s)$ is invariant under the basic matrix manipulations. For adding or subtracting two matrices this is obvious. For $\boldsymbol{G}(s) = \boldsymbol{Z}(s)\boldsymbol{Y}(s)$ it follows from (5) and (6) that (8) and (9) are the resulting elements of

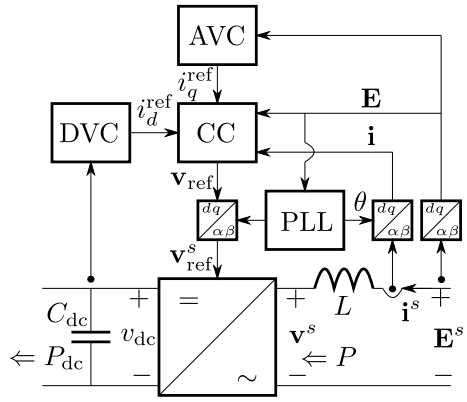

Fig. 2. VSC circuit diagram and control system.

$\boldsymbol{G}(s)$. Inverting a matrix in the form (12), e.g., to obtain the admittance corresponding to an impedance, yields

$$\boldsymbol{G}^{-1}(s) = \begin{bmatrix} \mathbf{G}_{-1}(s) & \tilde{\mathbf{G}}_{-1}(s) \\ \tilde{\mathbf{G}}^*_{-1}(s) & \mathbf{G}^*_{-1}(s) \end{bmatrix} \tag{14}$$

where $\mathbf{G}_{-1}(s) = \mathbf{G}^*(s)/[\mathbf{G}(s)\mathbf{G}^*(s) - \tilde{\mathbf{G}}(s)\tilde{\mathbf{G}}^*(s)]$ and $\tilde{\mathbf{G}}_{-1}(s) = -\tilde{\mathbf{G}}(s)/[\mathbf{G}(s)\mathbf{G}^*(s) - \tilde{\mathbf{G}}(s)\tilde{\mathbf{G}}^*(s)]$. Finally, transposing a matrix in the form (12) gives $\tilde{\mathbf{G}}(s) \to \tilde{\mathbf{G}}^*(s)$ and corresponds to trading places between the blocks $(\cdot)^*$ and $\tilde{\mathbf{G}}(s)$ in Fig. 1(a).

C. Application to Modeling of Grid-Connected VSCs

A grid-connected VSC can be modeled as an asymmetric input admittance as observed from the PCC [2], [12]. From the control laws that normally are used for grid-connected VSCs, the admittance parts $\mathbf{Y}(s)$ and $\tilde{\mathbf{Y}}(s)$ can be derived without intermediately using a real-vector MIMO model (as done in [2]). This modeling closely follows [12]. Yet there is the need for clarification, since in [12] attention is paid only to the derivation of $\mathbf{Y}(s)$, not $\tilde{\mathbf{Y}}(s)$; see the Appendix for details.

1) Control-System Structure: The VSC control system under consideration is depicted in Fig. 2. The ac-side circuit is referred to the $\alpha\beta$ frame—denoted by the superscript s—whereas the control system is implemented in the dq frame. The quantities correspond as $\mathbf{i}^s = e^{j\theta}\mathbf{i}$, etc., where θ is the dq-frame angle and $\mathbf{i}$ is the converter input current. The converter input filter is approximated as purely inductive, with inductance L. Four control loops are incorporated: the current controller (CC), the phase-locked loop (PLL), the direct-voltage controller (DVC), and the alternating-voltage controller (AVC).

The CC is given by the control law

$$\mathbf{v}_{\mathrm{ref}} = \mathbf{F}_c(s)(\mathbf{i} - \mathbf{i}_{\mathrm{ref}}) - j\omega_1 L\mathbf{i} + \mathbf{H}(s)\mathbf{E} \tag{15}$$

where $\mathbf{v}_{\mathrm{ref}}$ is the reference for the converter-voltage $\mathbf{v}$, the two related by the linear model $\mathbf{v} = \mathbf{G}_l(s)\mathbf{v}_{\mathrm{ref}}$ for the converter latency [24], $\mathbf{i}_{\mathrm{ref}} = i_d^{\mathrm{ref}} + ji_q^{\mathrm{ref}}$ is the reference for $\mathbf{i}$, term $-j\omega_1 L\mathbf{i}$ is the dq decoupler, and ω_1 is the fundamental angular frequency. Unlike [12], but similar to [2], feedforward through the low-pass filter $\mathbf{H}(s)$ [with $\mathbf{H}(0) = 1$] of the PCC voltage $\mathbf{E}$ is included. A proportional (P) controller $\mathbf{F}_c(s)$ is the core

to which an integral (I) part and/or resonant parts can be added, as desired.

The PLL computes the dq-frame angle as

$$\theta = \frac{1}{s}[F_p(s)\mathrm{Im}\{\mathbf{E}\} + \omega_1] \tag{16}$$

where a PI controller $F_p(s)$, possibly cascaded with a low-pass filter to suppress disturbances such as harmonics, is generally employed.

The DVC controls the direct (dc-link) voltage v_{dc} via the dc-link energy $W_{\mathrm{dc}} = (C_{\mathrm{dc}}/2)v_{\mathrm{dc}}^2$, where C_{dc} is the dc-link capacitance, using the control law

$$i_d^{\mathrm{ref}} = F_d(s)(W_{\mathrm{dc}}^{\mathrm{ref}} - W_{\mathrm{dc}}). \tag{17}$$

Controller $F_d(s)$ is often structurally similar, perhaps even identical, to $F_p(s)$.

The AVC controls the PCC-voltage magnitude via the law

$$i_q^{\mathrm{ref}} = F_a(s)(E_0 - |\mathbf{E}|) \tag{18}$$

where E_0 is the PCC-voltage magnitude reference. $F_a(s)$ may be a PI controller, possibly purely P or purely I, depending on the situation. A low-pass filter can—or, rather, should—be included in cascade, particularly if a P part is used.

2) Input Admittance: From the control laws (15)–(18), expressions for the input admittance parts $\mathbf{Y}(s)$ and $\tilde{\mathbf{Y}}(s)$ can be derived by adding up the individual contributions, as detailed in the Appendix. The result is

$$\mathbf{Y}(s) = \mathbf{Y}_c(s) + \mathbf{Y}_p(s) + \mathbf{G}_c(s)\mathbf{Y}_d(s) + \mathbf{Y}_a(s) \tag{19}$$

$$\tilde{\mathbf{Y}}(s) = -\mathbf{Y}_p(s) + \mathbf{G}_c(s)\mathbf{Y}_d^*(s) + \mathbf{Y}_a(s) \tag{20}$$

where

$$\mathbf{G}_c(s) = \frac{\mathbf{G}_l(s)\mathbf{F}_c(s)}{sL + j\omega_1 L[1 - \mathbf{G}_l(s)] + \mathbf{G}_l(s)\mathbf{F}_c(s)} \tag{21}$$

$$\mathbf{Y}_c(s) = \frac{1 - \mathbf{G}_l(s)\mathbf{H}(s)}{sL + j\omega_1 L[1 - \mathbf{G}_l(s)] + \mathbf{G}_l(s)\mathbf{F}_c(s)} \tag{22}$$

$$\mathbf{Y}_p(s) = -\frac{1}{2}[\mathbf{Y}_c(s) - \mathbf{G}_c(s)\mathbf{i}_0/E_0]G_p(s) \tag{23}$$

$$\mathbf{Y}_d(s) = -\frac{1}{2}[\mathbf{Y}_c(s) + \mathbf{i}_0^*/E_0]G_d(s) \tag{24}$$

$$\mathbf{Y}_a(s) = -j\frac{1}{2}\mathbf{G}_c(s)F_a(s). \tag{25}$$

Here, $\mathbf{G}_c(s)$ and $\mathbf{Y}_c(s)$ are respectively the closed-loop system and the input-admittance contribution of the CC. Equations (23), (24), and (25) quantify the input-admittance contributions of the PLL, DVC, and AVC, respectively. In (23) and (24), $G_p(s)$ and $G_d(s)$ are respectively the closed-loop systems of the PLL and the DVC, given as

$$G_p(s) = \frac{E_0 F_p(s)}{s + E_0 F_p(s)} \qquad G_d(s) = \frac{\kappa E_0 F_d(s)}{s + \kappa E_0 F_d(s)} \tag{26}$$

where $\kappa = 3/(2K^2)$ and K is the space-vector scaling constant.[2] Normally, the controllers are designed so that the bandwidths of $G_p(s)$ and $G_d(s)$ are substantially lower than that of $\mathbf{G}_c(s)$.

[2] $\kappa = 1$ for power-invariant scaling ($K = \sqrt{3/2}$) or normalization to per-unit quantities.

In (19) and (20) it can be noted that, being symmetric, the CC affects only $\mathbf{Y}(s)$. Neglecting the latency, i.e., $\mathbf{G}_l(s) = 1$, $\mathbf{G}_c(s)$ and $\mathbf{Y}_c(s)$ become real for a real $\mathbf{F}_c(s)$. This property is fundamental for reducing the complexity of real MIMO models, since a diagonal admittance matrix with relatively simple expressions is obtained [2]. Complex models obviate this issue; a complex $\mathbf{F}_c(s)$—resulting, e.g., from the addition of reduced-order generalized integrators [12]—poses no further difficulties.

Conversely, the PLL, DVC, and AVC, having an asymmetric impact, affect both $\mathbf{Y}(s)$ and $\tilde{\mathbf{Y}}(s)$.

Remark 3: Equations (19) and (20) simplify under certain, but often realistic, assumptions. First, since $\mathbf{G}_c(s)$ has high bandwidth, $\mathbf{G}_c(s) \approx 1$ within the much lower bandwidths of $G_p(s)$ and $G_d(s)$. This allows putting $\mathbf{G}_c(s) = 1$ in (19), (20), and (23). Second, converters are often operated at or near unity power factor, allowing $i_{q0} = 0$ to be assumed. Third, the PLL and DVC closed-loop bandwidths are often selected in the same range. So, with the final assumption that $G_d(s) = G_p(s)$, we get $\mathbf{Y}_p(s) = -[\mathbf{Y}_c(s) - i_{d0}/E_0]G_p(s)/2$ and $\mathbf{Y}_d(s) = -[\mathbf{Y}_c(s) + i_{d0}/E_0]G_p(s)/2$, giving

$$\mathbf{Y}(s) = \mathbf{Y}_c(s)[1 - G_p(s)] + \mathbf{Y}_a(s) \tag{27}$$

$$\tilde{\mathbf{Y}}(s) = -(i_{d0}/E_0)G_p(s) + \mathbf{Y}_a(s). \tag{28}$$

A considerable simplification is obtained. It can be noted that $\mathbf{Y}(s)$ becomes operating-point independent, because the PLL and DVC contributions that are proportional to i_{d0} cancel in (19), whereas in (20) they add constructively.

D. Passivity Properties and Passivity Index

Studying the passivity (dissipative) properties of an asymmetric system is particularly useful for the input admittance of a grid-connected VSCs [2]. For $Y(s)$ in the real-vector MIMO model (2), they are quantified via the eigenvalues $p_Y(\omega)$ of $A(\omega) = (1/2)[Y(j\omega) + Y^H(j\omega)]$ [23]. If the minimum eigenvalue $p_Y^{\min}(\omega)$—here called the passivity index[3]—is nonnegative, $Y(s)$ is dissipative for that ω. From (13) it follows that $Y(j\omega) + Y^H(j\omega) = \boldsymbol{T}^{-1}[\boldsymbol{Y}(j\omega) + \boldsymbol{Y}^H(-j\omega)]\boldsymbol{T}$. Consequently, for the complex-vector MIMO model,[4] the passivity index is found as the minimum eigenvalue of $\boldsymbol{A}(\omega) = (1/2)[\boldsymbol{Y}(j\omega) + \boldsymbol{Y}^H(-j\omega)]$, whose elements are given as

$$\boldsymbol{A}(\omega) = \frac{1}{2}\begin{bmatrix} \mathbf{Y}(j\omega) + \mathbf{Y}^*(-j\omega) & \tilde{\mathbf{Y}}(j\omega) + \tilde{\mathbf{Y}}(-j\omega) \\ \tilde{\mathbf{Y}}^*(j\omega) + \tilde{\mathbf{Y}}^*(-j\omega) & \mathbf{Y}^*(j\omega) + \mathbf{Y}(-j\omega) \end{bmatrix}. \tag{29}$$

After simplification, the following expression in the components of $\mathbf{Y}(s)$ and $\tilde{\mathbf{Y}}(s)$ is obtained:

$$p_Y^{\min}(\omega) = \mathrm{Re}\{Y_d(j\omega)\} - \sqrt{[\mathrm{Im}\{Y_q(j\omega)\}]^2 + [\mathrm{Re}\{\tilde{Y}_d(j\omega)\}]^2 + [\mathrm{Re}\{\tilde{Y}_q(j\omega)\}]^2}. \tag{30}$$

From the standpoint of closed-loop stability, see Section III, it is generally beneficial if the regions of negative passivity

[3] Note the difference relative [23], where the passivity index is instead defined as the ultimate minimum $\min_\omega p_Y(\omega)$.

[4] A way of calculating the passivity index for the complex-vector SISO model is yet to be found.

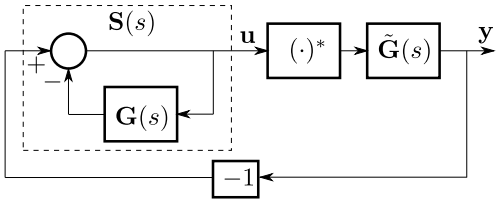

Fig. 3. Closed-loop system in Fig. 1(a) redrawn as a symmetric inner loop and an antisymmetric outer loop.

index are as narrow as possible [2]. In this respect, (30) is instructive, as it shows explicitly that only the d component of the symmetric part, more specifically the real part thereof, can contribute to a positive passivity index. All other parts can only contribute negatively.

Remark 4: Equations (27) and (28) are illustrative concerning the VSC input-admittance passivity properties under the assumptions stated in Remark 3. They show that only the CC, via $\mathbf{Y}_c(s)$, can contribute to a positive passivity index. The minus sign of $G_p(s)$ in (27) indicates that the PLL and the DVC contribute negatively, increasingly so with higher bandwidth [2]. As $\mathbf{G}_c(s)$ is predominantly real, $\mathbf{Y}_a(s)$ is predominantly imaginary and, thus, adds to $Y_q(s)$ and $\tilde{Y}_q(s)$, implying a negative contribution from the AVC. Somewhat different properties are obtained when $G_d(s) \neq G_p(s)$, on the other hand. For example, (23) and (24) indicate that, by making the bandwidth of $G_p(s)$ much larger than that of $G_d(s)$, a positive contribution in rectifier mode ($i_{d0} > 0$) can be obtained. Conversely, the opposite selection of the bandwidths gives a positive contribution in inverter mode ($i_{d0} < 0$).

III. Closed-Loop Stability Analysis

By including the dashed lines in Fig. 1, a closed-loop system is obtained. This is a generic model for any asymmetric system that uses negative feedback, but grid-connected VSCs are the foremost application. Three alternative stability analysis methods are considered in this section.

A. Method 1, Two-Loop Representation of the SISO Model

Fig. 1(a) can be redrawn as two cascaded feedback loops, as shown in Fig. 3. These loops are mathematical abstractions rather than physical control loops, but they allow the stability impacts of $\mathbf{G}(s)$ and $\tilde{\mathbf{G}}(s)$ to be analyzed separately. Closing the symmetric inner loop forms the sensitivity function [11]

$$\mathbf{S}(s) = \frac{1}{1+\mathbf{G}(s)}. \tag{31}$$

The stability of (31) can obviously be evaluated by applying the NC to the return ratio $\mathbf{G}(s)$. For a complex transfer function, the response for $\omega > 0$ is not generally the conjugate of that for $\omega < 0$. Consequently, evaluation for $s = j\omega$ over $-\infty < \omega < \infty$ is required, giving a Nyquist curve which generally is not symmetric about the real axis.

The antisymmetric outer loop can be further simplified as shown in Fig. 4(a), giving $\mathbf{u} = -\mathbf{G}_a(s)\mathbf{u}^*$, where

$$\mathbf{G}_a(s) = \tilde{\mathbf{G}}(s)\mathbf{S}(s) = \frac{\tilde{\mathbf{G}}(s)}{1+\mathbf{G}(s)}. \tag{32}$$

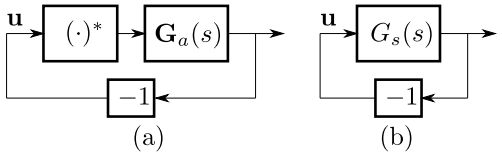

Fig. 4. (a) Antisymmetric outer loop with $\mathbf{G}_a(s) = \tilde{\mathbf{G}}(s)\mathbf{S}(s)$. (b) Equivalent symmetric outer loop with $G_s(s) = -\mathbf{G}_a(s)\mathbf{G}_a^*(s)$.

Conjugating $\mathbf{u} = -\mathbf{G}_a(s)\mathbf{u}^*$ yields $\mathbf{u}^* = -\mathbf{G}_a^*(s)\mathbf{u}$, and, thus, by eliminating $\mathbf{u}^*$ among the two relations, $\mathbf{u} = \mathbf{G}_a(s)\mathbf{G}_a^*(s)\mathbf{u}$. That is, the antisymmetric outer loop can be resolved into a symmetric loop as illustrated in Fig. 4(b). The stability of this loop can be assessed by applying the NC to the return ratio

$$G_s(s) = -\mathbf{G}_a(s)\mathbf{G}_a^*(s). \tag{33}$$

Note that $\mathbf{G}_a(s)\mathbf{G}_a^*(s)$ has real coefficients, which is why $G_s(s)$ does not have bold-letter notation.

Method 1 offers some valuable insight. Poor stability margins of $\mathbf{G}(s)$ give a small minimum distance from the Nyquist curve to the critical point -1, the inverse being the sensitivity peak $|\mathbf{S}(j\omega)|_{\max}$. Since $\mathbf{S}(s)$ appears as a factor in $G_s(s)$, the sensitivity peak expands the Nyquist curve of $G_s(s)$, likely reducing its stability margins. Thus, if $\mathbf{G}(s)$ and $\tilde{\mathbf{G}}(s)$ can be shaped, primary focus should be the stability margins of $\mathbf{G}(s)$, since they affect both loops. Examples are given in Section IV.

Remark 5: If $\mathbf{G}(s)$ and $\tilde{\mathbf{G}}(s)$ both are stable, the total closed-loop system is guaranteed to be asymptotically stable if the Nyquist curves for $\mathbf{G}(s)$ and $G_s(s)$ both avoid encirclement of -1. This requirement is conservative, however, as there may be cases where the inner loop is unstable [i.e., the Nyquist curve for $\mathbf{G}(s)$ encircles -1 clockwise], but the total system is stabilized by the outer loop [i.e., the Nyquist curve for $G_s(s)$ encircles -1 counterclockwise]. An example thereof is given in Section IV.

B. Method 2, Eigenvalue GNC Variant Applied to the MIMO Model

By considering the MIMO model (12), the stability of the closed-loop system obtained by the dashed lines in Fig. 1(b) can be analyzed by applying the GNC. The eigenvalue GNC variant [10] is closest in spirit to the NC and involves evaluating the eigenvalues $\lambda(s)$ of the matrix return ratio $\boldsymbol{G}(s)$. Plotting them for $s = j\omega$ gives the so-called characteristic loci, which, taken together, form the Nyquist curve. Solving for $\lambda(s)$ in the characteristic equation $|\lambda(s)I - \boldsymbol{G}(s)| = 0$, where I is the identity matrix, yields

$$\begin{aligned}\lambda(s) &= G_d(s) \pm \sqrt{\tilde{\mathbf{G}}(s)\tilde{\mathbf{G}}^*(s) - G_q^2(s)} \\ &= G_d(s) \pm j\underbrace{G_q(s)\sqrt{1 - \frac{\tilde{\mathbf{G}}(s)\tilde{\mathbf{G}}^*(s)}{G_q^2(s)}}}_{G_q'(s)}.\end{aligned} \tag{34}$$

Since $\tilde{\mathbf{G}}(s)\tilde{\mathbf{G}}^*(s)$ has real coefficients, so has $G_q'(s)$. Let $\lambda_{1,2}(s)$ respectively correspond to the plus and minus signs

in (34). We have $\lambda_1(-j\omega) = G_d(-j\omega) + jG'_q(-j\omega) = G^*_d(j\omega) + jG'^*_q(j\omega) = [G_d(j\omega) - jG'_q(j\omega)]^*$. This is the mirror image in the real axis of $\lambda_2(j\omega) = G_d(j\omega) - jG'_q(j\omega)$. Consequently, instead of evaluating both characteristic loci for $\omega > 0$, it is sufficient to evaluate $\lambda_1(j\omega)$, i.e., the plus sign in (34), for $-\infty < \omega < \infty$—the same crossings of the Nyquist curve with the real axis are obtained, but symmetry about the real axis is lost. For this sake, bold-letter notation is used in the following equivalent expression for λ_1:

$$\boldsymbol{\lambda}(s) = \mathbf{G}(s) + jG_q(s)\left[\sqrt{1 - \frac{\tilde{\mathbf{G}}(s)\tilde{\mathbf{G}}^*(s)}{G_q^2(s)}} - 1\right]. \quad (35)$$

This expression is instructive, as it involves adding a term to $\mathbf{G}(s)$, i.e., the return ratio of the inner loop in Method 1. The mentioned term vanishes for $\tilde{\mathbf{G}}(s) = 0$. Unlike Method 1, it is sufficient to plot one Nyquist curve, that for $\boldsymbol{\lambda}(s)$.

C. Method 3, Determinant GNC Variant Applied to the MIMO Model

Here, stability is verified if the Nyquist curve for the determinant of the return difference $I + \boldsymbol{G}(s)$ does not encircle the origin [11]. This is equivalent to avoidance of encirclement of -1 by the Nyquist curve for

$$\gamma(s) = |I + \boldsymbol{G}(s)| - 1. \quad (36)$$

We immediately obtain

$$\begin{aligned}\gamma(s) &= [1 + \mathbf{G}(s)][1 + \mathbf{G}^*(s)] - \tilde{\mathbf{G}}(s)\tilde{\mathbf{G}}^*(s) - 1 \\ &= \mathbf{G}(s) + \mathbf{G}^*(s) + \mathbf{G}(s)\mathbf{G}^*(s) - \tilde{\mathbf{G}}(s)\tilde{\mathbf{G}}^*(s). \quad (37)\end{aligned}$$

As in Method 2, an addition to $\mathbf{G}(s)$ is made, but it is such that $\gamma(s)$ has real coefficients; hence, its notation in italics.

Remark 6: Interestingly, (37) can be derived from Fig. 4(b) as follows. The characteristic equation for the closed-loop system is given by $1 + G_s(s) = 1 - \mathbf{G}_a(s)\mathbf{G}^*_a(s) = 0$, with $\mathbf{G}_a(s) = \tilde{\mathbf{G}}(s)/[1 + \mathbf{G}(s)]$

$$1 - \frac{\tilde{\mathbf{G}}(s)\tilde{\mathbf{G}}^*(s)}{[1 + \mathbf{G}(s)][1 + \mathbf{G}^*(s)]} = 0. \quad (38)$$

Multiplying by $[1+\mathbf{G}(s)][1+\mathbf{G}^*(s)]$ now yields $1+\gamma(s) = 0$, with $\gamma(s)$ given by (37).

D. Application to Stability Analysis of Grid-Connected VSCs

Connecting a VSC, with input-admittance parts given by (19) and (20), to an asymmetric grid, with impedance parts $\mathbf{Z}(s)$ and $\tilde{\mathbf{Z}}(s)$, gives the circuit model shown in Fig. 5. The grid voltage $\mathbf{V}_g$ is considered constant. Since the VSC input admittance is obtained via linearization and is operating-point dependent, a constant current source $\mathbf{i}_0$ is added to $\mathbf{i}$. The circuit is represented by the complex-vector SISO model

$$\mathbf{i} = \mathbf{Y}(s)\mathbf{E} + \tilde{\mathbf{Y}}(s)\mathbf{E}^* + \mathbf{i}_0 \quad (39)$$

$$\mathbf{E} = \mathbf{V}_g - [\mathbf{Z}(s)\mathbf{i} + \tilde{\mathbf{Z}}(s)\mathbf{i}^*] \quad (40)$$

This is an impedance–admittance cascade connection similar to (5) and (6), with the additions of $\mathbf{i}_0$ and $\mathbf{V}_g$. Transfer functions $\mathbf{G}(s)$ and $\tilde{\mathbf{G}}(s)$ of the cascade connection are obtained according to (8) and (9). Since $\mathbf{V}_g$ and $\mathbf{i}_0$ are constant, they do not impact the system stability. Considering $\mathbf{V}_g = \mathbf{i}_0 = 0$ reduces the closed-loop system to the SISO and MIMO models illustrated in Fig. 1 (dashed lines included).

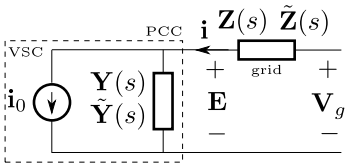

Fig. 5. VSC with asymmetric input admittance connected to a grid with asymmetric impedance.

1) Passive Grid Impedance: In many cases, the grid impedance is resistive–inductive–capacitive, implying that it is passive, i.e., it has a nonnegative passivity index for all frequencies. Then, as shown in [23], the Nyquist curve for the MIMO return ratio $\boldsymbol{G}(s) = \boldsymbol{Z}(s)\boldsymbol{Y}(s)$ cannot encircle -1 for ω where $p_Y^{\min}(\omega) \geq 0$. Consequently, in all three stability analysis methods under consideration, evaluation for ω where $p_Y^{\min}(\omega) < 0$ is sufficient. In addition, for Method 1, while a high sensitivity peak may lead to diminishing stability margins of the outer loop, it does not pose an instability risk if located where $p_Y^{\min}(\omega) \geq 0$.

IV. Numerical Examples

To compare the three methods for stability analysis of Section III, a VSC as modeled in Section II-C is considered. The grid impedance is considered as symmetric and, unless noted otherwise, purely inductive, $\mathbf{Z}(s) = (s + j\omega_1)L_g$, with $L_g = 1$ per unit (p.u.), i.e., a short-circuit ratio of 1. This represents a difficult operating condition for which instability phenomena easily occur.

For the converter filter, $L = 0.1$ p.u., which is reasonable, at least for converters of higher power and voltage ratings. The CC, PLL, and DVC use pure P controllers, parametrized as

$$\mathbf{F}_c(s) = \alpha_c L \qquad F_p(s) = \frac{\alpha_p}{E_0} \qquad F_d(s) = \frac{\alpha_d}{\kappa E_0} \quad (41)$$

respectively giving the closed-loop systems $\mathbf{G}_c(s) = \alpha_c/(s + \alpha_c)$, $G_p(s) = \alpha_p/(s + \alpha_p)$, and $G_d(s) = \alpha_d/(s + \alpha_d)$. The PCC-voltage feedforward filter is selected as $\mathbf{H}(s) = \mathbf{G}_c(s)$. In the three examples that follow, $\alpha_c = 5$ p.u., whereas α_p, α_d, and the AVC are detailed in the later in the text. The operating points $E_0 = 1$ p.u. and $\mathbf{i}_0 = i_{d0} = 0.8$ p.u. are considered. The latency is neglected, i.e., $\mathbf{G}_l(s) = 1$, since the properties at higher frequencies are not studied.

A. Example 1: Identical PLL and DVC Dynamics, Without AVC

Here, $\mathbf{F}_a(s) = 0$, while two different values of $\alpha_d = \alpha_p$ are considered: 0.4 p.u. and 0.588 p.u. The following observations can be made by inspecting Figs. 6 and 7.

- All three methods correctly show that $\alpha_d = \alpha_p = 0.588$ p.u. gives the boundary to instability. For Method 1, the outer loop turns unstable.

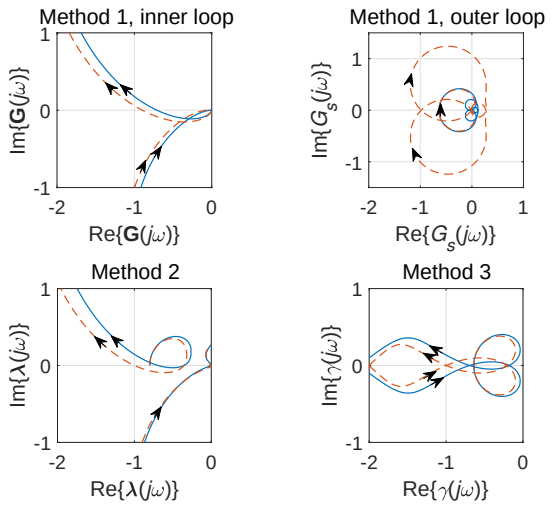

Fig. 6. Example 1: Nyquist curves for (solid) $\alpha_d = \alpha_p = 0.4$ p.u. and (dashed) $\alpha_d = \alpha_p = 0.588$ p.u.

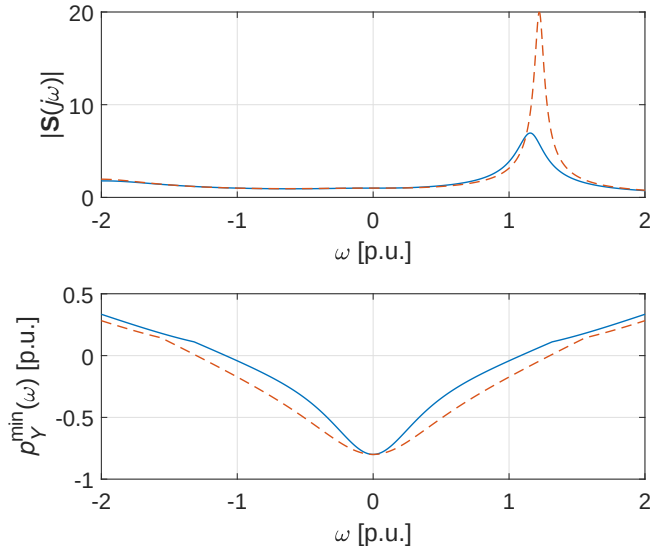

Fig. 7. Example 1: Sensitivity function and input-admittance passivity index for (solid) $\alpha_d = \alpha_p = 0.4$ p.u. and (dashed) $\alpha_d = \alpha_p = 0.588$ p.u.

- Method 1 gives continuous Nyquist curves which are easy to interpret.
- Method 2 results in a discontinuous Nyquist curve. A comparison indicates that this curve incorporates information from both curves of Method 1.
- Method 3 gives a convoluted Nyquist curve with numerous crossings of the negative real axis, making interpretation more difficult.
- The top plot of Fig. 7 indicates that the root cause for destabilization of the outer loop in Method 1 is the significant increase of the sensitivity peak obtained when changing $\alpha_d = \alpha_p$ from 0.4 p.u. to 0.588 p.u., accounting for the expansion of the Nyquist curve for the outer loop.
- The bottom plot of Fig. 7 shows that the negative-passivity-index region about $\omega = 0$ widens when $\alpha_d = \alpha_p$ is increased from 0.4 p.u. to 0.588 p.u. This has the effect that the sensitivity peak falls into the negative-passivity-index region—an indication of stability problems [2].

To compare $\boldsymbol{\lambda}(j\omega)$ as given by (35) with the characteristic loci $\lambda_{1,2}\{\boldsymbol{G}(j\omega)\}$ (all evaluated for $-\infty < \omega < \infty$), the latter are overlayed the former in Fig. 8(a) and the displayed area is enlarged relative Fig. 6. As can be observed, both curves convey the same information, the latter with symmetry about the real axis.

Fig. 8(b) depicts the full plots of $\boldsymbol{\lambda}(j\omega)$ and $\gamma(j\omega)$, showing that the latter is much wider than the former; roughly $|\gamma(j\omega)| \sim |\boldsymbol{\lambda}(j\omega)|^2$ for large ω. This is the result of term $\mathbf{G}(s)\mathbf{G}^*(s)$ in (37), which causes the multiple crossings of the negative real axis as well.

B. Example 2: Different PLL and DVC Dynamics, With AVC

In this example, the claim of Remark 4 that the PLL can give a positive contribution to the passivity index for $i_{d0} > 0$ is put to test by letting $\alpha_p = 1$ p.u. and $\alpha_d = 0.1$ p.u. That is, the PLL is now ten times faster than the DVC. In addition, AVC with $F_a(s) = K_a\alpha_a/(s+\alpha_a)$, $K_a = 2$ p.u., (i.e., P with low-pass filter) is included. Two different values of bandwidth α_a are used: 0.1 p.u. and 0.487 p.u., the latter which gives the boundary to instability. Comparing the solid curves in Fig. 9 to those in Fig. 6, increased stability margins can be observed. These can be correlated to the reduced width of the negative-passivity-index region in Fig. 10 relative Fig. 7.

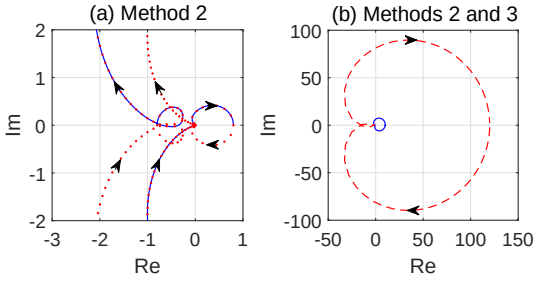

Fig. 8. Example 1: Nyquist curves for $\alpha_d = \alpha_p = 0.4$ p.u. (a) (solid) $\boldsymbol{\lambda}(j\omega)$ and (dotted) characteristic loci of $\boldsymbol{G}(j\omega)$. (b) (solid) $\boldsymbol{\lambda}(j\omega)$ and (dashed) $\gamma(j\omega)$.

Increasing the bandwidth of the AVC filter gives instability (dashed curves). For Method 1, now the inner loop turns unstable (although the outer loop is close to being unstable, too). This results in an infinite sensitivity peak, see the top plot of Fig. 10.

C. Example 3: Identical PLL and DVC Dynamics, Without AVC, With Grid Resonance

The inductive grid impedance is modified to an inductive–capacitive parallel impedance with the $\alpha\beta$-frame angular resonant frequency $\omega_{\text{res}} = 1/\sqrt{L_g C_g}$. For the control loops, $\alpha_d = \alpha_p = 0.4$ p.u. and $F_a(s) = 0$. Two different resonant frequencies are considered, 5.0 p.u. and 2.36 p.u.

In Fig. 11, all three methods immediately show stability for $\omega_{\text{res}} = 5.0$ p.u. Methods 2 and 3 do so for $\omega_{\text{res}} = 2.36$

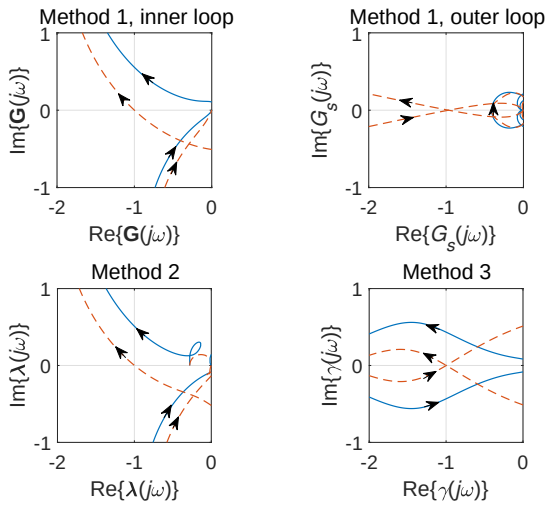

Fig. 9. Example 2: Nyquist curves for (solid) $\alpha_a = 0.1$ p.u. and (dashed) $\alpha_a = 0.487$ p.u.

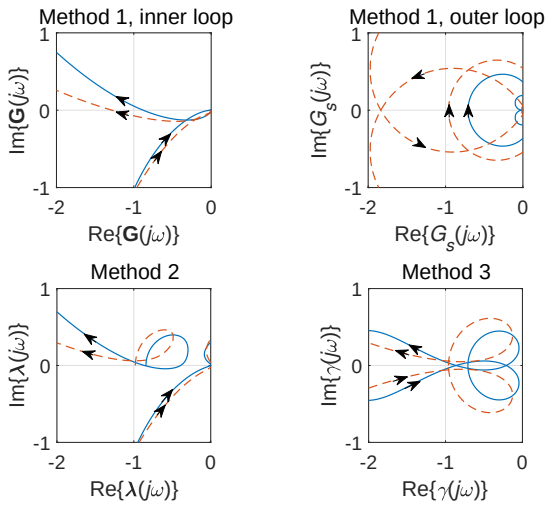

Fig. 11. Example 3: Nyquist curves for (solid) $\omega_{\rm res} = 5.0$ p.u. and (dashed) $\omega_{\rm res} = 2.36$ p.u.

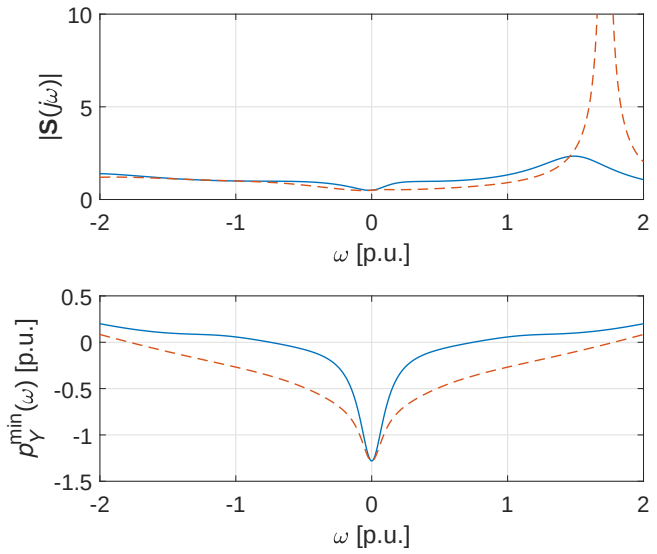

Fig. 10. Example 2: Sensitivity function and input-admittance passivity index for (solid) $\alpha_a = 0.1$ p.u. and (dashed) $\alpha_a = 0.487$ p.u.

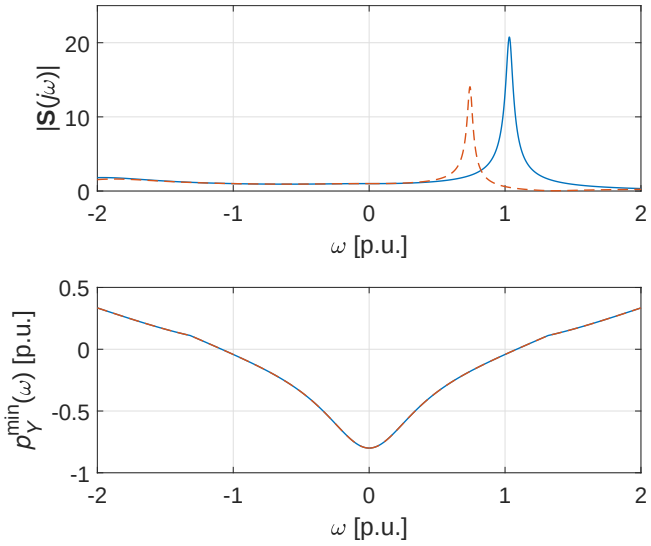

Fig. 12. Example 3: Sensitivity function and input-admittance passivity index for (solid) $\omega_{\rm res} = 5.0$ p.u. and (dashed) $\omega_{\rm res} = 2.36$ p.u.

p.u. as well. However, Method 1 too shows stability, since the dashed Nyquist curve for the inner loop encircles -1 clockwise, whereas that for the outer loop makes the encirclement counterclockwise. The outer loop stabilizes the unstable inner loop. This finding is of importance. Since the PLL and DVC dynamics are identical, $\mathbf{Y}(s)$ is operating-point invariant, whereas $\tilde{\mathbf{Y}}(s)$ is proportional to $-i_{d0}$, see (27) and (28). Consequently, the stability is conditional of the operating point $i_{d0} = 0.8$ p.u. For example, if instead $i_{d0} = 0$, then $\tilde{\mathbf{Y}}(s) = 0 \Rightarrow \mathbf{G}_a(s) = 0 \Rightarrow G_s(s) = 0$, and the outer loop no longer stabilizes the inner loop.

The aggravated situation for the case $\omega_{\rm res} = 2.36$ p.u. can be correlated to the sensitivity peak coinciding with $p_{\rm Y}^{\rm min}(\omega) < 0$, see Fig. 12. Even though the sensitivity peak for $\omega_{\rm res} = 5.0$ p.u. is higher, it is merely on the boundary of the negative-passivity-index region.

1) Experimental Results: The case $\omega_{\rm res} = 2.36$ p.u. is verified experimentally using a VSC with ratings 7 kVA, 200 V (rms), and 50 Hz. The sampling and switching frequencies are both 10 kHz, using a dSPACE DS1007 system where voltage and current measurement is made by a DS2004 high-speed analog-to-digital board. Gate signals are generated using a DS5101 digital waveform output board. The parameters are identical to those of the theory; in addition, there are obviously losses in the circuit that are not accounted for in the model. Fig. 13 shows the PCC phase voltage and the converter phase current, for the same phase. (The curve of the latter, which initially has the larger amplitude, is shown with a sign change.) As can be observed, initially, where the dc-link load power $P_{\rm dc}$ is set so as to give $\mathbf{i} = 0.8$ p.u., the system is stable. In the center of the displayed time interval, $P_{\rm dc}$ is zeroed, resulting in the current decaying to zero. In accordance with the finding of Method 1 that the stability is conditional of the operating

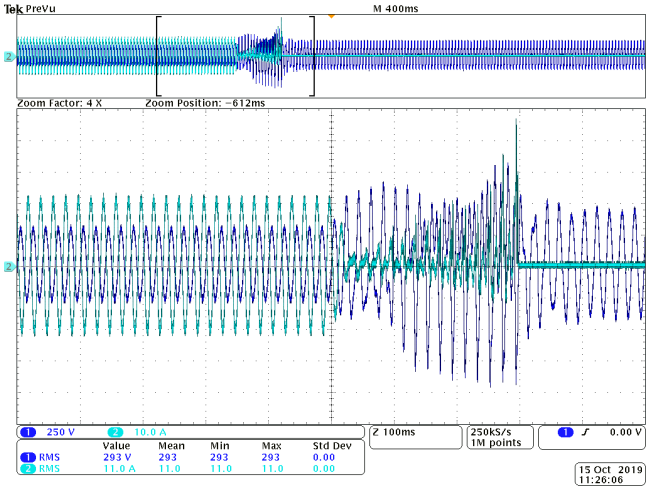

Fig. 13. Example 3: Experimental verification for $\omega_{\rm res} = 2.36$ p.u. In the center of the displayed time interval, $P_{\rm dc}$ is zeroed, resulting in $i_{d0} = 0$ and instability.

point $i_{d0} = 0.8$ p.u., this results in instability and subsequent tripping of the converter.

Remark 7: In [12], it is argued that stability often can be (approximately) assessed by considering just the symmetric part of Fig. 1(a), i.e., the inner loop of Method 1. This is corroborated by the finding in Section III that the stability margins of the inner loop, via the sensitivity function $\mathbf{S}(s)$, affect the outer loop as well. In all three examples shown here, when at or close to instability (dashed curves), indeed the Nyquist curves for both loops show very poor stability margins. Examining the inner loop only may give results that are either slightly optimistic (as in Example 1), exact (as in Example 2), or slightly pessimistic (as in Example 3) concerning stability. Yet, it is advisable to examine both loops, as there may be cases where the results deviate from these findings.

V. Conclusions

Modeling and analysis of asymmetric systems using complex-vector SISO and MIMO models was considered. Both models carry the same information and are, thus, complimentary. The main usage for the MIMO model is for calculating results that cannot be obtained using the SISO model.

One benefit of the approach is that direct complex-vector modeling of asymmetric systems is facilitated, where the real- and imaginary-part operators give contributions to both the symmetric and antisymmetric parts.

Another benefit is that complex transfer functions can be used for closed-loop stability analysis—particularly as applied to grid-connected VSCs—avoiding matrix manipulations. In this respect, three candidate methods for stability analysis were presented and evaluated.

Method 1 (two-loop representation) shows that the stability margins of the inner loop affect also those of the outer loop, via the sensitivity function. Two Nyquist curves need to be plotted; yet, it is in general easy to assess stability. Exceptions are certain close-to-instability cases, where the curves for the inner and outer loops may encircle -1 respectively clockwise and counterclockwise.

In Method 2 (eigenvalue GNC variant), one Nyquist curve suffices. Its interpretation, including realistic stability margins, is straightforward.

Method 3 (determinant GNC variant), on the other hand, is less useful, since the resulting Nyquist curve often is convoluted with multiple crossings of the negative real axis.

Appendix

The input-admittance contributions of the CC, PLL, DVC, and AVC are here derived.

The effect of the CC can be calculated by combining the relation $(s+j\omega_1)L\mathbf{i} = \mathbf{E} - \mathbf{v}$ obtained from Fig. 2 with (15) and the latency model $\mathbf{v} = \mathbf{G}_l(s)\mathbf{v}_{\rm ref}$, giving

$$\mathbf{i} = \mathbf{G}_c(s)\mathbf{i}_{\rm ref} + \mathbf{Y}_c(s)\mathbf{E} \tag{42}$$

where the expressions for the transfer functions are given in (21) and (22).

The PLL gives a dynamic impact via the dq transformations of $\mathbf{i}^s$ and $\mathbf{E}^s$ as well as via the $\alpha\beta$ transformation of $\mathbf{v}_{\rm ref}$. This impact is nonlinear and the technique for its linearization is well studied in the literature, e.g., [12]. In brief, parametrization in operating points and perturbation quantities is made as $\mathbf{i}^s = e^{j\omega_1 t}(\mathbf{i}_0 + \Delta\mathbf{i})$, $\mathbf{E}^s = e^{j\omega_1 t}(E_0 + \Delta\mathbf{E})$, and $\mathbf{v}^s_{\rm ref} = e^{j\omega_1 t}(\mathbf{v}_0 + \Delta\mathbf{v}_{\rm ref})$ [since the PLL aligns the dq frame along $\mathbf{E}^s$, E_0 is real; evaluating (15) statically gives $\mathbf{v}_0 = E_0 - j\omega_1 L\mathbf{i}_0$]. Similarly, $\theta = \omega_1 t + \Delta\theta$, allowing the dq and $\alpha\beta$ transformations to be linearized according to the principle $\mathbf{i} = e^{-j\theta}\mathbf{i}^s \approx (1 - j\Delta\theta)(\mathbf{i}_0 + \Delta\mathbf{i}) \approx \mathbf{i}_0 + \Delta\mathbf{i} - j\mathbf{i}_0\Delta\theta$. This results in the substitutions

$$\mathbf{i} \to \mathbf{i} - j\mathbf{i}_0\Delta\theta \quad \mathbf{E} \to \mathbf{E} - jE_0\Delta\theta \quad \mathbf{v}_{\rm ref} \to \mathbf{v}_{\rm ref} + j\mathbf{v}_0\Delta\theta \tag{43}$$

to be made in (15) to account for the PLL impact. Solving for $\mathbf{i}$ results in the addition of $j[\mathbf{G}_c(s)\mathbf{i}_0 - E_0\mathbf{Y}_c(s)]\Delta\theta$ to (42). Eliminating $\Delta\theta$ by substituting (43) in (16) yields $\omega_1 t + \Delta\theta = [F_p(s){\rm Im}\{E_0 + \Delta\mathbf{E} - jE_0\Delta\theta\} + \omega_1]/s$, from which $\Delta\theta$ is solved as

$$\Delta\theta = G_p(s){\rm Im}\{\Delta\mathbf{E}\}/E_0 \tag{44}$$

where $G_p(s)$, given in (26), represents the closed-loop PLL dynamics. Since ${\rm Im}\{\Delta\mathbf{E}\} = {\rm Im}\{\mathbf{E}\} = (\mathbf{E} - \mathbf{E}^*)/(2j)$, accounting for the PLL impact implies adding $\mathbf{Y}_p(s)(\mathbf{E} - \mathbf{E}^*)$ to (42), where $\mathbf{Y}_p(s)$ is given in (23).

To calculate the DVC impact, the converter is approximated as lossless. Fig. 2 yields the power balance $W_{\rm dc} = (P - P_{\rm dc})/s$. Substituting this relation in (17) and expressing the result in perturbation quantities (where $\Delta W^{\rm ref}_{\rm dc} = \Delta P_{\rm dc} = 0$) gives

$$\Delta i_d^{\rm ref} = -\frac{F_d(s)}{s}\Delta P. \tag{45}$$

Linearizing the relation $P = \kappa{\rm Re}\{\mathbf{E}\mathbf{i}^*\}$ for the active input power yields $\Delta P = \kappa{\rm Re}\{E_0\Delta\mathbf{i}^* + \mathbf{i}_0^*\Delta\mathbf{E}\} = \kappa{\rm Re}\{E_0\Delta\mathbf{i} + \mathbf{i}_0^*\Delta\mathbf{E}\}$, from which $\Delta\mathbf{i}$ is eliminated by substituting (42) (with perturbation quantities), giving

$$\Delta P = \kappa{\rm Re}\{E_0\mathbf{G}_c(s)\Delta\mathbf{i}_{\rm ref} + [E_0\mathbf{Y}_c(s) + \mathbf{i}_0^*]\Delta\mathbf{E}\}. \tag{46}$$

In this process, the PLL impact on ΔP is neglected, which for most purposes represents a minor approximation. The CC and the DVC are normally tuned so that the closed-loop dynamics of $\mathbf{i}$ are much faster than those of $W_{\rm dc}$. Yet, owing to the control law (17), $i_d^{\rm ref}$ evolves on the time scale of $W_{\rm dc}$. This motivates considering $\mathbf{G}_c(s) = 1$ in (46), which yields the simplification $\mathrm{Re}\{E_0\mathbf{G}_c(s)\Delta\mathbf{i}_{\rm ref}\} = E_0\Delta i_d^{\rm ref}$. Now, by substituting (46) in (45), the following simple solution of $\Delta i_d^{\rm ref}$ is obtained:

$$\Delta i_d^{\rm ref} = -G_d(s)\mathrm{Re}\{[\mathbf{Y}_c(s) + \mathbf{i}_0^*/E_0]\Delta\mathbf{E}\} \qquad (47)$$

where $G_d(s)$ is given in (26). An equivalent expression for (47) is $\Delta i_d^{\rm ref} = \mathbf{Y}_d(s)\Delta\mathbf{E} + \mathbf{Y}_d^*(s)\Delta\mathbf{E}^*$, where $\mathbf{Y}_d(s)$ is given in (24). Substitution in (42), dropping the distinction of perturbation quantities, it is found that the DVC impact is accounted for by adding $\mathbf{G}_c(s)[\mathbf{Y}_d(s)\mathbf{E} + \mathbf{Y}_d^*(s)\mathbf{E}^*]$ to (42).

For the AVC, in (18), $|\mathbf{E}| \approx \mathrm{Re}\{\mathbf{E}\}$, since the dq frame is aligned with $\mathbf{E}^s$. Thus, (18) in perturbation quantities becomes $\Delta i_q^{\rm ref} = -F_a(s)\mathrm{Re}\{\Delta\mathbf{E}\}$, so the AVC impact is found simply by adding $\mathbf{Y}_a(s)(\mathbf{E} + \mathbf{E}^*)$ to (42), where $\mathbf{Y}_a(s)$ is given in (25).

REFERENCES

[1] L. Harnefors, "Modeling of three-phase dynamic systems using complex transfer functions and transfer matrices," *IEEE Trans. Ind. Electron.*, vol. 54, no. 4, pp. 2239–2248, Aug. 2007.

[2] L. Harnefors, M. Bongiorno, and S. Lundberg, "Input-admittance calculation and shaping for controlled voltage-source converters," *IEEE Trans. Ind. Electron.*, vol. 54, no. 6, pp. 3323–3334, Dec. 2007.

[3] K. D. T. Ngo, "Low frequency characterization of PWM converters," *IEEE Trans. Power Electron.*, vol. PE-1. no. 1, pp. 223–230, Oct. 1986.

[4] M. Belkhayat, "Stability criteria for AC power systems with regulated loads," Ph.D. thesis, Purdue University, West Lafayette, IN, Dec. 1997.

[5] S. Hiti, D. Boroyevich, and C. Cuadros, "Small-signal modeling and control of three-phase PWM converters," in *Proc. IEEE Ind. Appl. Soc. Annu. Meeting*, Oct. 1994.

[6] Z. Liu, J. Liu, W. Bao, and Y. Zhao, "Infinity-norm of impedance-based stability criterion for three-phase ac distributed power systems with constant power loads," *IEEE Trans. Power Electron.*, vol. 30, no. 6, pp. 3030–3043, Jun. 2015.

[7] B. Wen, D. Boroyevich, R. Burgos, P. Mattavelli and Z. Shen, "Small-signal stability analysis of three-phase ac systems in the presence of constant power loads based on measured d-q frame impedances," *IEEE Trans. Power Electron.*, vol. 30, no. 10, pp. 5952–5963, Oct. 2015.

[8] B. Wen, D. Boroyevich, R. Burgos, P. Mattavelli, and Z. Shen, "Analysis of D-Q small-signal impedance of grid-tied inverters," *IEEE Trans. Power Electron.*, vol. 31, no. 1, pp. 675–687, Jan. 2016.

[9] T. Roinila, T. Messo, and E. Santi, "MIMO-identification techniques for rapid impedance-based stability assessment of three-phase systems in DQ domain," *IEEE Trans. Power Electron.*, vol. 33, no. 5, pp. 4015–4022, May 2018.

[10] I. Postlethwaite and A. G. J. MacFarlane, *A complex variable approach to the analysis of linear multivariable feedback systems.* Berlin, Germany: Springer-Verlag, 1979.

[11] S. Skogestad and I. Postlethwaite, *Multivariable Feedback Control: Analysis and Design.* Chichester: Wiley, 1996.

[12] L. Harnefors, X. Wang, A. G. Yepes, and F. Blaabjerg, "Passivity-based stability assessment of grid-connected VSCs—An overview," *IEEE J. Emerg. Sel. Top. Power Electron.*, vol. 4, no. 1, Mar. 2016, pp. 116–125.

[13] A. Rygg, M. Molinas, C. Zhang, and X. Cai, "A modified sequence-domain impedance definition and its equivalence to the dq-domain impedance definition for the stability analysis of AC power electronic systems," *IEEE J. Emer. Sel. Top. Power Electron.*, vol. 4, no. 4, pp. 1383–1396, Dec. 2016.

[14] A. Rygg, M. Molinas, C. Zhang, and X. Cai, "On the equivalence and impact on stability of impedance modeling of power electronic converters in different domains," *IEEE J. Emer. Sel. Top. Power Electron.*, vol. 5, no. 4, pp. 1444–1454, Dec. 2017.

[15] C. Zhang, X. Cai, A. Rygg, and M. Molinas, "Sequence domain SISO equivalent models of a grid-tied voltage source converter system for small-signal stability analysis," *IEEE Trans. Energy Convers.*, vol. 33, no. 2, pp. 741–749, Jun. 2018.

[16] C. Zhang, M. Molinas, A. Rygg, and X. Cai, "Impedance-based analysis of interconnected power electronics systems: Impedance network modeling and comparative studies of stability criteria," *IEEE J. Emer. Sel. Top. Power Electron.*, early access, 2019.

[17] X. Wang, L. Harnefors, and F. Blaabjerg, "Unified impedance model of grid-connected voltage-source converters," *IEEE Trans. Power Electron.*, vol. 33, no. 2, pp. 1775–1787, Feb. 2017.

[18] H. Zhang, L. Harnefors, X. Wang, H. Gong, J.-P. Hasler, and H.-P. Nee, "SISO transfer functions for stability analysis of grid-connected voltage-source converters," *IEEE Trans. Ind. Appl.*, vol. 55, no. 3, pp. 2931–2941, May–Jun. 2019.

[19] H. Zhang, L. Harnefors, X. Wang, H. Gong, and J.-P. Hasler, "Stability analysis of grid-connected voltage-source converters using SISO modeling," *IEEE Trans. Power Electron.*, vol. 34, no. 8, pp. 8104–8117, Aug. 2019.

[20] J. M. Undrill and T. E. Kostyniak, "Subsynchronous oscillations part I – comprehensive system stability analysis," *IEEE Trans. Power Appar. Syst.*, vol. PAS-95, no. 4, pp. 1446-1455, Jul./Aug. 1976.

[21] M. W. Degner and C. M. Wolf, "Transient analysis of asymmetric AC systems using complex vectors," in *Proc. IEEE IEMDC*, Miami, FL, May 2017.

[22] S. Shah and L. Parsa, "Impedance modeling of three-phase voltage source converters in dq, sequence, and phasor domains," *IEEE Trans. Energy Conv.*, vol. 32, no. 3, pp. 1139–1150, Sep. 2017.

[23] J. Bao, P. L. Lee, F. Wang, and W. Zhou, "New robust stability criterion and robust controller synthesis," *Int. J. Robust Nonlinear Control*, vol. 8, pp. 49–59, 1998.

[24] L. Harnefors, R. Finger, X. Wang, H. Bai, and F. Blaabjerg, "VSC input-admittance modeling and analysis above the Nyquist frequency for passivity-based stability assessment," *IEEE Trans. Ind. Electron.*, vol. 64, no. 8, pp. 6362–6370, Aug. 2017.

Lennart Harnefors (S'93–M'97–SM'07–F'17) received the M.Sc., Licentiate, and Ph.D. degrees in electrical engineering from the Royal Institute of Technology (KTH), Stockholm, Sweden, and the Docent (D.Sc.) degree in industrial automation from Lund University, Lund, Sweden, in 1993, 1995, 1997, and 2000, respectively. Between 1994–2005, he was with Mälardalen University, Västerås, Sweden, from 2001 as a Professor of electrical engineering. Between 2001–2005, he was, in addition, a part-time Visiting Professor of electrical drives with Chalmers University of Technology, Göteborg, Sweden. In 2005, he joined ABB, HVDC Product Group, Ludvika, Sweden, where he led the control development for cascaded-two-level-converter HVDC Light. In 2012, he joined ABB, Corporate Research, Västerås, Sweden, where he was appointed as a Senior Principal Scientist in 2013. He is, in addition, a part-time Adjunct Professor of power electronics with KTH since 2011.

Dr. Harnefors is an Associate Editor of *IET Electric Power Applications*. He was certified as a 2018 Outstanding Reviewer of the IEEE TRANSACTIONS ON POWER ELECTRONICS. His research interests include control and dynamic analysis of power electronic systems, particularly grid-connected converters and ac drives.

Xiongfei Wang (S'10–M'13–SM'17) received the B.S. degree from Yanshan University, Qinhuangdao, China, in 2006, the M.S. degree from Harbin Institute of Technology, Harbin, China, in 2008, both in electrical engineering, and the Ph.D. degree in energy technology from Aalborg University, Aalborg, Denmark, in 2013. Since 2009, he has been with the Department of Energy Technology, Aalborg University, where he became an Assistant Professor in 2014, an Associate Professor in 2016, a Professor and Research Program Leader for Electronic Power Grid (eGrid) in 2018, and the Director of Aalborg University–Huawei Energy Innovation Center in 2020. His current research interests include modeling and control of grid-interactive power converters, stability and power quality of converter-based power systems, active and passive filters.

Dr. Wang was selected into Aalborg University Strategic Talent Management Program in 2016. He has received six IEEE Prize Paper Awards, the 2016 Outstanding Reviewer Award of the IEEE TRANSACTIONS ON POWER ELECTRONICS, the 2018 IEEE PELS Richard M. Bass Outstanding Young Power Electronics Engineer Award, the 2019 IEEE PELS Sustainable Energy Systems Technical Achievement Award, and the 2019 Highly Cited Researcher by Clarivate Analytics (formerly Thomson Reuters). He serves as a Member at Large for Administrative Committee of IEEE Power Electronics Society 2020–2022, and as an Associate Editor for the IEEE TRANSACTIONS ON POWER ELECTRONICS, the IEEE TRANSACTIONS ON INDUSTRY APPLICATIONS, and the IEEE JOURNAL OF EMERGING AND SELECTED TOPICS IN POWER ELECTRONICS.

Shih-Feng Chou (S'09–M'17) received the B.S. and M.S. degrees in electrical engineering from National Tsing Hua University, Hsinchu, Taiwan, in 2009 and 2011, respectively. He performed R&D in power electronics for renewable energy systems with Delta Electronics, Inc., Taoyuan, Taiwan, from 2012 to 2017. Since 2017, he was a research assistant in the department of energy technology in Aalborg University, Aalborg, Denmark, where he is currently working toward the Ph.D. degree. His research focuses on modeling of large-scale power electronics based power system.

Massimo Bongiorno (S'02–M'07–SM'16) received the M.Sc. degree in electrical engineering from the University of Palermo, Palermo, Italy, in April 2002, and the Lic.Eng. and Ph.D. degrees from the Chalmers University of Technology, Gothenburg, Sweden, in December 2004 and September 2007, respectively. From 2007 to 2010, he was an Assistant Professor at the Department of Electric Power Engineering, Chalmers University of Technology, where he became an Associate Professor in 2010. Since 2015, he has been holding the position of Professor in power electronic applications for power systems. His research interests include application of power electronics in power systems, power system dynamics, and power quality.

Marko Hinkkanen (M'06–SM'13) received the M.Sc.(Eng.) and D.Sc.(Tech.) degrees in electrical engineering from the Helsinki University of Technology, Espoo, Finland, in 2000 and 2004, respectively. He is currently an Associate Professor with the School of Electrical Engineering, Aalto University, Espoo, Finland. His research interests include control systems, electric drives, and power converters.

Dr. Hinkkanen was a General Co-Chair for the 2018 IEEE 9th International Symposium on Sensorless Control for Electrical Drives (SLED). He received the 2016 International Conference on Electrical Machines (ICEM) Brian J. Chalmers Best Paper Award and the 2016 and 2018 IEEE Industry Applications Society Industrial Drives Committee Best Paper Awards. He is an Associate Editor for the IEEE TRANSACTIONS ON ENERGY CONVERSION and *IET Electric Power Applications*.

Mikko Routimo (M'18) received the M.Sc.(Eng.), Lic.Tech., and D.Sc.(Tech.) degrees in electrical engineering from Tampere University of Technology, Tampere, Finland, in 2002, 2005, and 2009, respectively. Since 2008, he has been with ABB, Drives, Helsinki, Finland, where he is currently a Principal Engineer. Since 2017, he has also been a Professor of Practice with the School of Electrical Engineering, Aalto University, Espoo, Finland. His research interests include power electronics in power systems, control of grid-connected converters, and electric drives.